Utilizing focused field as a probe for shape determination of subwavelength structures via coherent Fourier scatterometry

Paul, Anubhav; Wever, Robin; Soman, Sarika; Pereira, Silvania F.

DOI
10.1103/PhysRevApplied.23.024016

Publication date
2025

Document Version
Final published version

Published in
Physical Review Applied

Citation (APA)
Paul, A., Wever, R., Soman, S., & Pereira, S. F. (2025). Utilizing focused field as a probe for shape determination of subwavelength structures via coherent Fourier scatterometry. *Physical Review Applied*, *23*(2), Article 024016. https://doi.org/10.1103/PhysRevApplied.23.024016

PHYSICAL REVIEW APPLIED **23,** 024016 (2025)

Utilizing focused field as a probe for shape determination of subwavelength structures via coherent Fourier scatterometry

Anubhav Paul,[*] Robin Wever, Sarika Soman, and Silvania F. Pereira
Imaging Physics Department, Faculty of Applied Sciences, Delft University of Technology, Lorentzweg 1, Delft 2628 CJ, Netherlands

(Received 16 September 2024; revised 20 November 2024; accepted 2 December 2024; published 6 February 2025)

Nanopillars are widely used for various applications and require accurate shape characterization to enhance their performance and optimize fabrication processes. In this paper, we employ coherent Fourier scatterometry (CFS) combined with rigorous three-dimensional finite-difference time-domain simulations to accurately determine the shapes of nanopillars with various geometries, including cylindrical, triangular, square, and rectangular shapes. The nanopillars considered here have lateral dimensions (a) ranging from 100 to 1000 nm. Our methodology utilizes the preferential excitation of the nanostructures by a tightly focused beam and leverages their inherent symmetry to capture far-field signatures that vary periodically with rotation. This approach allows us to distinguish between different nanopillar shapes based on these rotational signatures. Our results demonstrate that the CFS method can reliably characterize nanopillars with lateral dimensions $a \geq 300$ nm, surpassing the conventional diffraction limit of 351 nm. However, the method reaches its fundamental limits for $a \leq 200$ nm, as also confirmed by simulations, where we approach the dipole approximation regime ($a \ll \lambda$). This constraint is not observed for rectangular nanopillars, owing to their constant breadth ($b = 1000$ nm), which prevents such a regime. Furthermore, our method successfully differentiates nanopillars transitioning from rectangular to square shapes. We also explored the method's limitations concerning nanostructure height (h), finding that triangular and square nanopillars could be characterized accurately for $h \geq 50$ nm and $h \geq 150$ nm, respectively. Furthermore, the method remains robust against shape distortions such as edge roundness. The method is primarily effective in determining the lateral (top-down) shape of nanopillars, it does not resolve longitudinal features. The ability to accurately characterize nanostructure shapes has significant implications in fields such as photonics and biosensing, where geometry critically influences device performance.

DOI: 10.1103/PhysRevApplied.23.024016

I. INTRODUCTION

Nanopillars, subwavelength structures with nanoscale dimensions, have gained significant attention across various fields due to their unique properties and wide range of applications, such as photonics [1–3], electronics [4], sensing [5–7], energy [8,9], and biotechnology [10,11]. These nanostructures have the ability to manipulate light and interact with matter at the nanoscale. The chemical and physical properties of nanopillars, such as electron mobility, band gaps, and crystal structure, have been shown to exhibit a strong dependence on their dimensions, specifically their diameter and length [12–14]. This dependence arises from various phenomena, including quantum confinement, and enhanced phonon scattering, which become prominent as the dimensions of the structures approach the nanoscale. In addition to size, the cross-sectional shape and overall geometry of nanopillars are also crucial factors influencing their properties. Recognizing this, researchers have optimized the shapes of nanopillars in the literature for specific applications, leading to designs, such as cylindrical, triangular, square, and rectangular cross sections [15–17]. However, despite these advancements, the fabrication of nanostructures with precise and tailored geometries remains a significant challenge [18–20]. The fabrication processes often result in cylindrical nanostructures, which may not always be ideal for all applications [21]. In the semiconductor industry, for instance, the presence of defects in wafer manufacturing can lead to substantial yield losses [22]. To identify the origin of the defects and ultimately control them, characterization of the presence, shape, size, and composition is needed. Therefore, the characterization of nanostructures,

---

[*] Contact author: A.Paul-1@tudelft.nl

particularly their shape, becomes essential not only for improving fabrication techniques but also for ensuring the desired functional properties of them in their respective applications.

While significant progress has been made in the characterization of the geometrical shapes of different nanostructures, much of this has focused on structures with dimensions larger than the illumination beam, such as step-phase objects defined by height and sidewall angles [23–25], or periodic structures like gratings [26–28]. However, characterizing the shape of isolated nanostructures having dimensions smaller than the illumination beam presents a considerable challenge due to the limitations imposed by Abbe's diffraction limit. This fundamental constraint restricts our ability to resolve and accurately visualize structures smaller than the wavelength of the illumination beam, making it difficult to characterize very small nanostructures. Recent studies have attempted to overcome this by extracting features from scattering patterns to classify or distinguish different shapes at the wavelength scale [29–31]. While these methods provide some insight into structural details, they fall short of offering accurate and independent determinations of the exact shapes of nanostructures, particularly for those smaller than the illumination beam and beyond the diffraction limit.

A variety of traditional tools have been employed to characterize the shape of nanostructures, which include scanning electron microscopy (SEM) [32], atomic force microscopy (AFM) [33], and scanning near-field optical microscopy (SNOM) [34]. Each tool has its own set of advantages and limitations, Both SEM and AFM are benchmark tools, offering high-resolution imaging. However, they have low throughput and can potentially inflict permanent damage to the sample, making them invasive and primarily employed in offline mode. SNOM can achieve resolution beyond the diffraction limit but is hampered by complex setup requirements, challenging data interpretation, and limited depth profiling due to the short propagation distance of near-field light. Scattering-based techniques have also been widely utilized for nanostructure characterization [35]. Critical dimension small angle x-ray scattering (CD-SAXS) [36] is highly effective for analyzing nanoscale dimensions with high precision but is constrained by the brightness of compact x-ray sources, which leads to long measurement times. Similarly, Mueller-matrix imaging ellipsometry (MMIE) [37] and Mueller-matrix scattered-field microscopy (MSM) [38] are powerful tools for extracting detailed information about the optical and geometrical properties of nanostructures. However, these methods often require advanced modeling and are typically constrained to periodic nanostructures. In contrast, coherent Fourier scatterometry (CFS) presents a more versatile approach that is not confined to periodic nanostructures and does not require complex modeling. CFS has been successfully applied to a range of problems, demonstrating its flexibility and effectiveness. For periodic structures, CFS has been used to retrieve grating parameters [28], as well as for detection of isolated subwavelength particles [39]. Moreover, CFS has shown its capability in hybrid scenarios, such as detecting an isolated defect within a periodic grating [40]. These applications highlight the potential of CFS as a robust and adaptable technique for characterizing both periodic and isolated nanostructures.

This paper presents a methodology based on CFS to determine the shapes of various nanopillars, including cylindrical, triangular, square, and rectangular geometries. By utilizing a focused beam for preferential excitation and the inherent symmetry of these nanostructures, we capture distinctive far-field signatures that vary with rotation, allowing us to determine the different shapes based on these rotational patterns. Our methodology breaks the diffraction limit while remaining robust against shape distortions, such as edge roundness. While our methodology can determine the lateral (top-down) shape of nanopillars, it has limitations in resolving longitudinal features. Despite the limitation, the ability to determine the lateral shape of nanostructures provides a crucial step for advancing the manufacturing of these nanostructures for applications in fields such as photonics and biosensing.

II. METHODS

A. Concept

In this section, we introduce the scattering problem and the associated diffraction theory for CFS. In Fig. 1(left) the scattering problem is schematically illustrated, where a subwavelength scatterer present on top of a substrate is illuminated by a focused laser beam. We introduce a coordinate system (x, y, z) at the focal plane to define the geometry of the scattering system. The position of the subwavelength scatterer is defined as the origin of this coordinate system. According to the angular spectrum decomposition formalism, the focused beam can be decomposed into an infinite number of plane waves of different propagation directions [41]. Each such instance of plane waves $U_i(\theta_i, \phi_i)$ will be scattered (U_s) by the scatterer and collected by the microscope objective (O) having numerical aperture (NA), which will be further propagated to the back focal plane (BFP) (having a different coordinate system (ξ, η)) based on the Fourier optics theory [42]. The mapping of the scattered beams in the BFP is constrained by the NA of the O.

A key aspect of our approach is the high NA (=0.9) illumination, which creates a nonsymmetric field in the focal region, as predicted by the vectorial diffraction theory [43,44]. This field is elongated along the polarization direction of the incident light. In Fig. 1(bottom right) the elongated electric field intensity in the focal plane is shown. In the case of $\mathrm{NA} = 0.9$, and wavelength

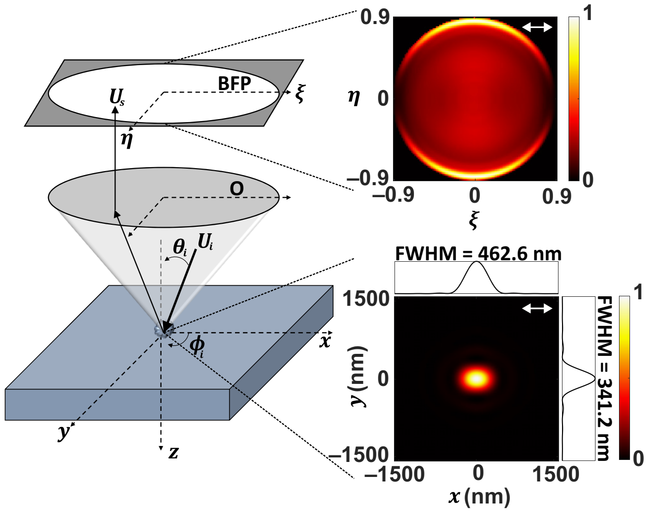

FIG. 1. (Left) Schematic representation of a subwavelength scatterer on a substrate illuminated by a focused laser beam. A plane wave (U_i) within the beam is scattered (U_s) and captured by a microscope objective (O) having numerical aperture (NA) and propagated to the back focal plane (BFP). (Bottom right) Electric field intensity in the focal plane that interacts with the scatterer. Cross-sections reveal the FWHM, indicating field elongation along the polarization direction. (Top right) Far-field image of a point scatterer illuminated by the focused field, consisting of two lobes, manifesting dipole radiation. Arrows denote the polarization direction.

$\lambda = 633$ nm, the electric field intensity along the polarization direction has FWHM = 462.2 nm, and for the electric field intensity orthogonal to the polarization direction, the FWHM = 341.2 nm. Let us consider a simple system where the nanostructure is a very small particle ($\ll \lambda$) and can be approximated to a single oscillating dipole. This approximation yields a characteristic far-field pattern with lobes oriented according to the polarization direction of the incident light [as shown in Fig. 1(top right)]. This is due to the asymmetry in the focal field, which induces a preferential excitation of the nanostructures along specific directions. Further, the scattering pattern deviates from this dipolelike behavior for larger or more complex nanostructures (here nanopillars of different shapes) where the single oscillating dipole approximation is not valid. This leads to additional features encoded in the far-field that provide more detailed information about the nanostructure. We aim to utilize this encoded information in the far-field signatures, where the asymmetry in the focal field induces a preferential excitation of the nanopillars along specific directions, combined with the intrinsic symmetry of the shape of the nanopillar. For this, we systematically rotate the nanopillars and analyze the resulting far-field patterns. By correlating these patterns with the nanostructure's orientation, we can infer the shape of the nanostructures.

B. Experimental setup

In this section, we outline the experimental setup for CFS, as depicted schematically in Fig. 2. A He-Ne laser operating at a wavelength of $\lambda = 633$ nm generates a collimated illumination beam, achieved through coupling with a single-mode fiber. Lens 1 couples the laser into the fiber, while lens 2 collimates the light emerging from it. A linear polarizer is used to control the polarization direction of the illumination beam. The polarizer can be rotated by an angle $\theta (= 0^\circ \text{ to } 360^\circ)$, where the position $\theta = 0^\circ$ is defined as that where the polarization direction at the pupil is parallel to the x axis. The linearly polarized collimated beam is directed through a nonpolarizing beam splitter and then focused onto the nanopillars on the sample using a high numerical aperture (NA = 0.9) microscope objective. The sample is mounted on a piezocontrolled translation stage (*XYZ* TS), to localize the nanopillars on the sample, allowing for precise observation. The scattered light is collected by the same microscope objective, passes back through the nonpolarizing beam splitter, and is then relayed to the back focal plane of the microscope objective via a telescopic system composed of lens 3 and lens 4. A CCD camera positioned at this plane captures the angular spectrum of the scattered waves from all incident plane waves within the focused spot.

In the experiments, rather than rotating the nanopillars, which is practically complex, we manually rotate the linear polarizer and perform a single-shot measurement with the CCD camera for each of the different polarization directions of the illumination beam, defined by θ. For each of these captured far-field images, we rotate these images back by an angle $-\theta$. This is done to imitate the situation where we rotate the nanopillars by θ. Further due to the reflection symmetry of the linear polarizer, the illumination beam for θ and $\theta + 180^\circ$ is identical. Hence we

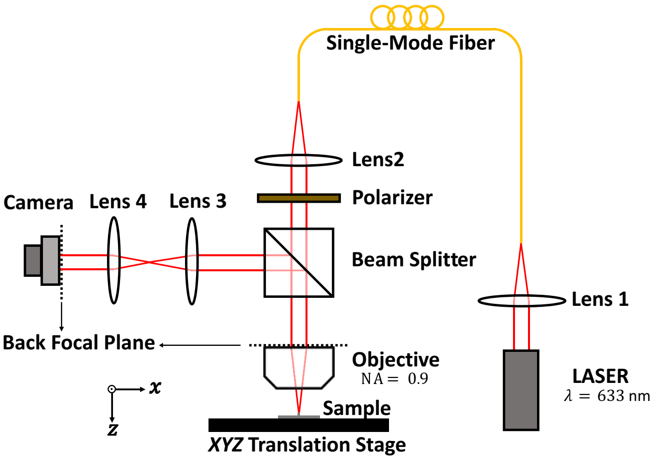

FIG. 2. Schematic of the experimental setup of coherent Fourier scatterometry (CFS).

perform only single-shot measurement for the polarization directions of the illumination beam at θ with, $\theta = \Delta\theta \times n$, where $\Delta\theta = 30^\circ$ and $n \in [0, 5] \cap \mathbb{Z}$.

C. Numerical model

The problem of the interaction between a tightly focused beam and nanopillars on a substrate is complex and demands careful consideration due to the intricate geometries and the presence of a substrate that disrupts the symmetry of the system [45]. Previous studies have primarily concentrated on the scattering of electromagnetic waves by spherical particles on flat surfaces, using various methods like Mie theory and the extensions of Weyl's method [46], and dipole approximations [47,48] to simplify the problem. However, when dealing with more complex shapes, these simplified models and assumptions are insufficient. The substrate's impact on the scattering becomes more pronounced, especially when dealing with nonspherical geometries. Therefore, to accurately model the interaction of a focused beam with these nanopillar structures, we utilized rigorous 3D electromagnetic simulations, the finite-difference time-domain (3D-FDTD) method, implemented with the commercial software package Lumerical FDTD [49]. This approach solves Maxwell's equations in the time domain by discretizing space (Yee grids) and time.

In the simulations, we replicate the experimental conditions by modeling an isolated nanopillar (centered at the origin on the xy plane) on top of a flat substrate, as the simulation object. The simulation domain is carefully sized to ensure that the width of the focused beam (FWHM approximately 462 nm) is much smaller than the simulation domain's dimension (=14 μm). To prevent reflections, we apply perfectly matched-layer (PML) boundary conditions on all boundaries. For the illumination, we utilize the vectorial diffraction theory of Richards and Wolf [43,50], employing a TM polarized (i.e., the polarization direction at the pupil is parallel to the x axis) plane wave of wavelength $\lambda = 633$ nm being focused by a microscope objective of numerical aperture 0.9 onto the focal plane (we choose our focal plane to be at the top of the substrate, i.e., $z = 0$ plane). The scattered near field from the nanopillar is calculated and sampled at a monitor plane, thereafter propagating it into the far field through the FDTD simulation [51].

In Fig. 3(a), the $y = 0$ plane, and in Fig. 3(b), the $z = 0$ plane of the complete 3D-FDTD model is depicted. The geometrical parameters, lateral dimension (a), and height (h) characterize the simulation object's geometry (here the case of square nanopillar for illustration). The nanopillar's and the substrate's material is silicon (Si) with a refractive index of $n = 3.88126 + 0.01894i$. To investigate the influence of rotation of the nanopillar on the far-field signatures, we systematically rotate the simulation object by an angle $\theta (= 0^\circ$ to $360^\circ)$, while keeping the position of the source injection plane, monitor plane, and computational domain constant. The position of the different nanopillars at $\theta = 0^\circ$ is shown in Fig. 3(c).

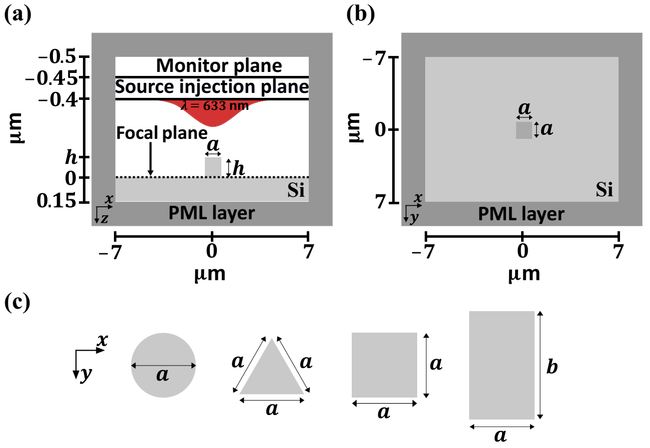

FIG. 3. Illustration of the 3D-FDTD model, where a nanopillar (square nanopillar) is illuminated by a TM-polarized focused beam of wavelength 633 nm (emanating from source injection plane). The scattered near field is sampled at the monitor plane and propagated to the far field through the FDTD simulation. (a) Corresponding $y = 0$ plane; (b) corresponding $z = 0$ plane; (c) the orientation of the different nanopillars at the $z = 0$ plane for $\theta = 0$.

D. Sample design and fabrication

A sample consisting of Si nanopillars of different shapes with nominal geometrical parameters as detailed in Table I is fabricated using e-beam lithography followed by etching. The Si wafer, after cleaning is spin coated with the ARN7520 resist at 4000 rpm followed by a pre-exposure bake at 85 °C for 60 sec. The design is written on the resist with an exposure dose of 500 mJ/cm^2 using the Raith EBPG5200. After exposure, the resist is developed in MF322 solution for 60 sec followed by rinsing in water. The structures are then etched using reactive ion etching in Sentech Etchlab 200. The remaining resist is stripped by sonicating the sample in acetone for 5 min. In Fig. 4 (top panel), we show the SEM image of the fabricated nanopillars of the different shapes. The +-shaped markers are fabricated to facilitate the localization of the nanopillars on the sample. In Fig. 4 (bottom panel), we show enlarged SEM images of the different nanopillars having nominal geometrical parameters: $a = 300$ nm, and $h = 250$ nm. The SEM measurements show that the lateral dimensions of the fabricated nanopillars are within 30 nm of the nominal values, however the tilted plane measurement of the nanopillars were not conclusive, and we cannot report the actual height of the fabricated nanopillars.

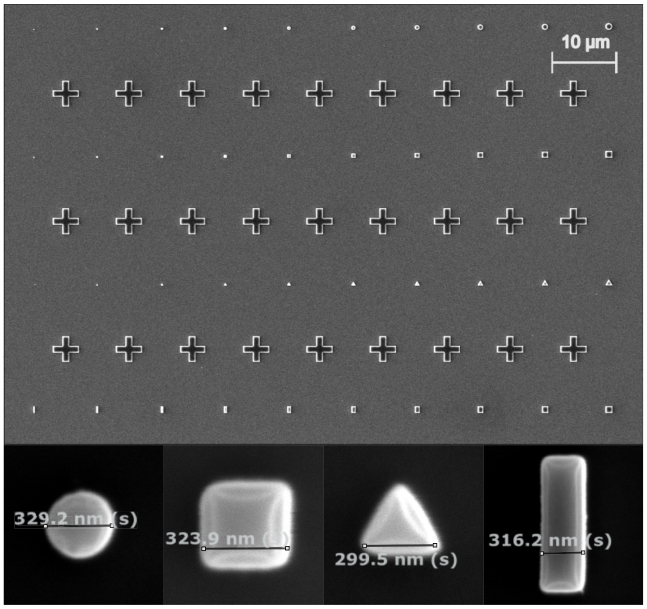

FIG. 4. (Top panel) SEM image of the fabricated nanopillars, described by geometrical parameters of Table I. The +-shaped markers are fabricated to facilitate the localization of the nanopillars on the sample. (Bottom panel) Enlarged SEM images of the different nanopillars.

III. RESULTS

A. Comparison of simulations and experiments

In this section, we compare our simulated results with experimental data. Simulations allow us to explore the limitations of the methodology by varying parameters that cannot be easily adjustable in experiments, enabling us to better understand the underlying physics. Therefore, we need to establish that the simulation results are consistent with the experimental data. To illustrate this, let us consider a triangular nanopillar of geometrical parameters defined by length $a = 500$ nm and height $h = 250$ nm. In Fig. 5(a), we show the simulated far-field signatures corresponding to different orientations of the triangular nanopillar, defined by the rotation of the nanopillar ($\theta = 0^\circ, 30^\circ$, and 60°). We observe a significant deviation of the far-field signatures from the symmetric dipolelike signature when a small spherical particle on a substrate interacts with a focused beam [39], and that the far-field signatures are different for the different θ, demonstrating that the far-field signatures are sensitive to the shape and orientation of the nanopillars even though the dimension of the nanopillars are smaller than the Airy diameter of the focused spot ($= 1.22\lambda/\mathrm{NA} = 858$ nm). In Fig. 5(b), we show the corresponding experimental far-field signatures, where instead of rotating the nanopillar sample we have rotated the polarization direction by θ and the far-field signatures have been rotated by $-\theta$. We observe that the simulated and experimental far-field signatures are consistent with each other demonstrating that our simulation model is faithful and that the combination of rotating the direction of polarization and the far-field signatures is equivalent to rotating the sample.

B. Determination of shapes of nanopillars

In this section, we demonstrate that the shape of subwavelength nanopillars can be retrieved by utilizing the influence of geometrical shape and orientation of the nanopillars on the far-field signatures. We aim to understand how the different orientations, i.e., the rotation of the nanopillars, will influence the far-field signatures and how they will differ for the different shapes. Now, to quantify these variations in the far-field signatures, we define a metric "$C_{A,B}$" which measures the correlation between the far-field signatures. With "$C_{A,B}$" mathematically expressed as

$$C_{A,B} = \frac{\sum_{i=1}^{N}\sum_{j=1}^{N}\left(A_{ij} - \bar{A}\right)\left(B_{ij} - \bar{B}\right)}{\sqrt{\left(\sum_{i=1}^{N}\sum_{j=1}^{N}\left(A_{ij} - \bar{A}\right)^2\right)\left(\sum_{i=1}^{N}\sum_{j=1}^{N}\left(B_{ij} - \bar{B}\right)^2\right)}}, \tag{1}$$

where, A_{ij} and B_{ij} are the two far-field signatures at the (i,j)th pixel, with N^2 being the total number of pixels in the square far-field plane. $\bar{A}$ and $\bar{B}$ are the mean of all the N^2 pixels in the far-field plane of A and B, respectively.

For the analysis, we consider all the different shapes of nanopillars defined by geometrical parameters, $a = 500$ nm, $b = 1000$ nm, and $h = 250$ nm. We systematically rotate each nanopillar by an angle defined by

TABLE I. Nominal geometrical parameters of the nanopillars.

Shape	Diameter/length a (nm)	Breadth b (nm)	Height h (nm)
Cylindrical nanopillar	$100, 200, \ldots, 1000$	…	250
Triangular nanopillar	$100, 200, \ldots, 1000$	…	250
Square nanopillar	$100, 200, \ldots, 1000$	…	250
Rectangular nanopillar	$100, 200, \ldots, 1000$	1000	250

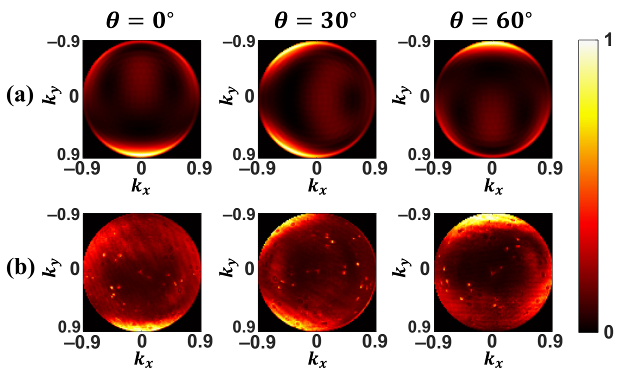

FIG. 5. Far-field signatures corresponding to different rotations θ ($= 0^\circ, 30^\circ$, and 60°) of the triangular nanopillar, defined by geometrical parameters: $a = 500$ nm and $h = 250$ nm. (a) Simulated using 3D-FDTD; (b) Experimental data.

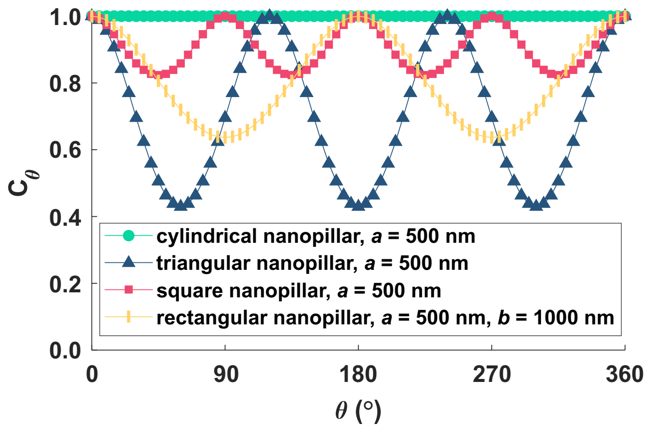

FIG. 6. Simulated variation in far-field signatures as a function of θ for different nanopillar shapes, quantified by the correlation metric $C_\theta (= C_{0,0+\theta})$ as defined by Eq. (1). The results demonstrate a periodic variation in C_θ depending on the symmetry of the nanopillar shapes. The nanopillars are characterized by geometrical parameters: $a = 500$ nm, $b = 1000$ nm, and $h = 250$ nm.

$\theta (\theta = 0^\circ$ to $360^\circ)$ and for each type of nanopillar we calculate the correlation metric "$C_\theta (= C_{\theta_0,\theta_0+\theta})$." With, $\theta_0 = 0^\circ$, and $\theta = 0^\circ$ to 360°. However, θ_0 can be chosen to be any other arbitrary angle as well. In Fig. 6, we show the variation in the far-field signatures for the different shapes of nanopillars. The curves of different shapes have markers of the corresponding shapes. We observe that all the nanopillars of different shapes display different periodicity in the correlation metric. We observe that the periodicity of the correlation metric varies for the different shapes of the nanopillars i.e., 120° for triangular nanopillar, 90° for square nanopillar, and 180° for rectangular nanopillar. This periodicity depends on the rotational symmetry of the shape of the nanopillar. For cylindrical nanopillar, we do not observe any periodicity in the correlation metric as the cylindrical nanopillar is identical for any rotation θ. Therefore, based on C_θ we can determine the shape of the different nanopillars. Further, we observe that the peak-to-peak of C_θ, of the different shapes of nanopillars is not the same and indicates that the influence of rotation of the nanopillars on the variation in the far-field signatures is most sensitive for the triangular nanopillar, followed by rectangular nanopillar, with the square nanopillar showing the least sensitivity.

Now, we demonstrate experimentally that by utilizing CFS one can determine the shape of all different shapes of nanopillars. Here, we measure the far-field signatures of all the fabricated nanopillars described by the geometrical parameters as shown in Table I. For each nanopillar, we systematically rotate the linear polarizer manually from $\theta = 0^\circ$ to 150° with a separation of 30°, following the description in Sec. II B. From all the far-field signatures measured, we calculate the correlation metric "$C_\theta (= C_{\theta_0,\theta_0+\theta})$," where $\theta_0 = 0^\circ, \theta = \Delta\theta \times n$, with $\Delta\theta = 30^\circ$ and $n \in [0, 12] \cap \mathbb{Z}$. In Fig. 7(a), we show the experimental variation of the correlation metric for cylindrical nanopillars. The correlation metric shows no periodicity for all the different dimensions a, indicating that these nanopillars are cylindrical. Further, we have $C_0 = C_{360} = 1$ as they are the same far-field signature and identical. However, for the other C_θ, it is not 1, this is because of experimental limitations, as it is not possible to guarantee that the nanopillar is at the exact center of the beam while we are taking the different measurements by rotating the linear polarizer manually. Further, there is the presence of multiple dirt particles in the microscope objective [can also be seen in the experimental far-field signatures of Fig. 5(b)], which appears in the far-field signatures, and as we rotate the far field by an angle $-\theta$, these specks of dirt also rotate and reduce the correlation between them. Furthermore, as the fabrication process is not ideal, the presence of surface roughness and the fact that nanopillars are not exactly symmetric, also contributes to the reduction in correlation between them. In Fig. 7(b), we show the experimental variation of the correlation metric for triangular nanopillars. The correlation metric shows a clear periodicity of 120° for the different dimensions a. In Fig. 7(c), we show the experimental variation of the correlation metric for square nanopillars. The correlation metric shows a clear periodicity of 90° for the different dimensions a. In Fig. 7(d), we show the experimental variation of the correlation metric for rectangular nanopillars. The correlation metric shows a clear periodicity of 180° for the different dimensions a. Further, it is interesting to observe the variation in the correlation metric for the situation where the rectangle is converting to a square i.e., for $a = 800$ nm (rectangle), 900 nm (rectangle), and 1000 nm (square) [shown in the inset of Fig. 7(d)]. For dimension, $a = 800$ nm (rectangle), the variation in correlation metric has a periodicity of 180°. For dimension $a = 900$ nm

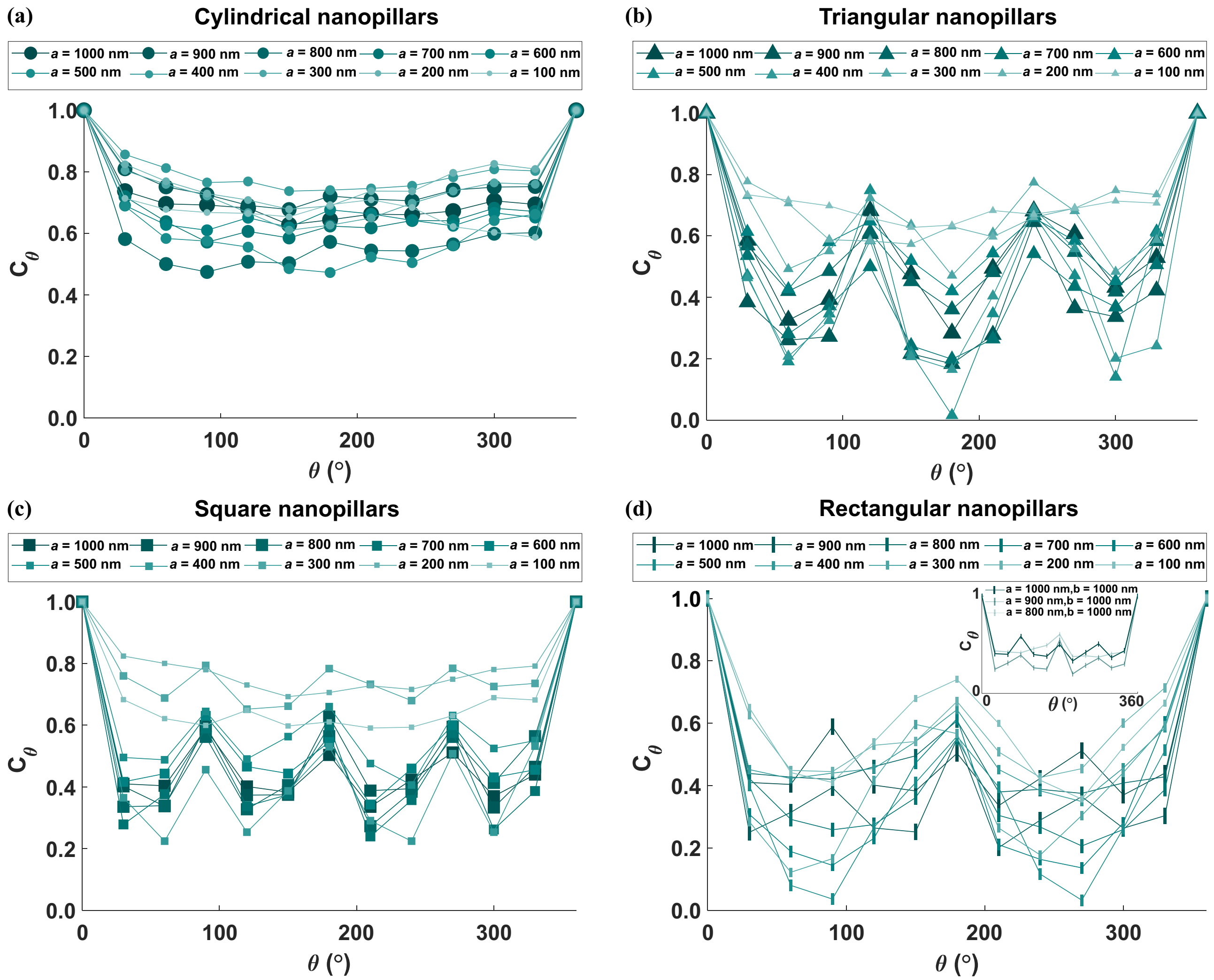

FIG. 7. Experimental variation in far-field signatures as a function of θ for the different fabricated nanopillars, quantified by the correlation metric $C_\theta (= C_{0,0+\theta})$ as defined by Eq. (1). The nanopillars are characterized by geometrical parameters as given by Table I. (a) For cylindrical nanopillars; (b) for triangular nanopillars; (c) for square nanopillars; (d) for rectangular nanopillars, with the inset showing the periodicity of the correlation metric C_θ changing from 180° for $a = 800$ nm (rectangle) to 90° for $a = 1000$ nm (square).

(rectangle), the variation in correlation metric has a periodicity of 180° but with small peaks appearing at $\theta = 90°$, and 270°. For dimension $a = 1000$ nm (square), the variation in correlation metric has a periodicity of 90°. These results imply that we can also distinguish the shape of the nanopillars, which are almost square to square in shape. This experiment demonstrates that by utilizing CFS we can experimentally determine the shape of the different nanopillars (cylindrical, triangular, square, and rectangular) in a model-independent manner beyond the diffraction limit (diffraction limit $= \lambda/2\text{NA} = 351$ nm).

C. Limitation of shape determination

In this section, we analyze the limitations of our methodology for determining the shape of nanopillars. As our methodology is based on scattering from the nanopillars, the limiting factors include the lateral dimension of nanopillars (a), the height of nanopillars (h), and the quality of the fabrication of the nanopillars. Accordingly, we define a quantitative metric "pk-to-pk C," which measures the maximum change in the correlation metric. The metric pk-to-pk C indicates the sensitivity of variation in the far-field signatures due to the rotation of the nanopillars. The metric pk-to-pk C can be mathematically expressed as

$$\text{pk-to-pk } C = \max|\text{loc}\max(C_\theta)| - \min|\text{loc}\min(C_\theta)|, \tag{2}$$

where $C_\theta (= C_{\theta_0,\theta_0+\theta})$ is the correlation metric as defined by Eq. (1), with $\theta_0 = 0°$, and $\theta \in (0°, 360°)$. With loc $\max(C_\theta) = C_{\theta_{\max}}$, $C_{\theta_{\max}} \geq C_\theta$ for all $\theta \in (\theta_{\max} - \delta, \theta_{\max} + \delta)$, loc $\min(C_\theta) = C_{\theta_{\min}}$, $C_{\theta_{\min}} \leq C_\theta$ for all $\theta \in (\theta_{\min}$

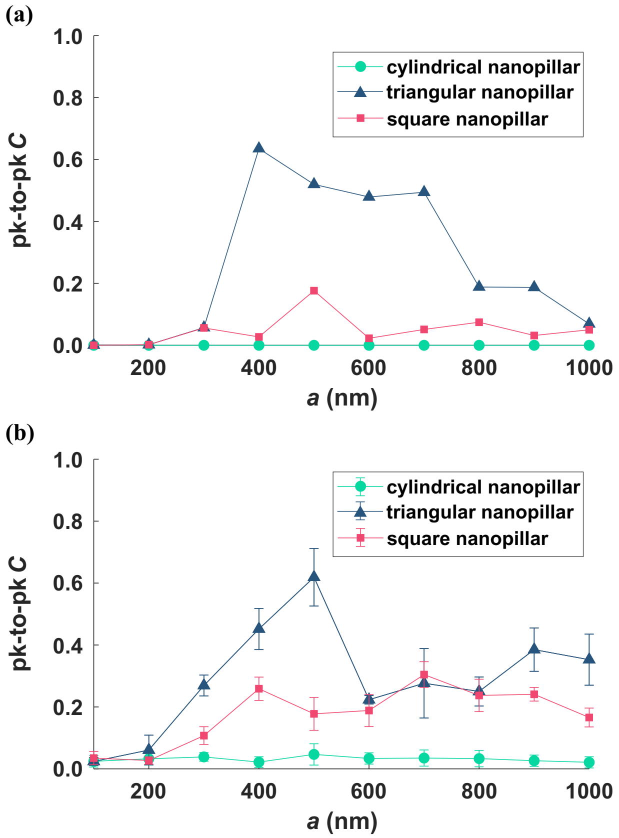

FIG. 8. Limitation analysis of the lateral dimension (a) of the nanopillars. (a) Simulated using 3D-FDTD; (b) experimental data. Both indicating that the shape of the nanopillars can be determined for $a \geq 300$ nm.

$-\delta, \theta_{\min}+\delta)$, and $\delta(\delta > 0)$ considers the immediate neighborhood of $\theta_{\max}, \theta_{\min}$. We exclude C_0 and C_{360} to emphasize on the relative variations in C_θ for nonidentical far-field signatures.

Now, we analyze the limitation of the proposed CFS method for the determination of the shape of the nanopillars against the lateral dimension (a) of the nanopillars. Accordingly, we systematically vary the lateral dimension of the nanopillars $a = 100$ nm to 1000 nm, for the different shapes of nanopillars (cylindrical, triangular, and square) with $h = 250$ nm. We measure the correlation "C_θ" and calculate the metric "pk-to-pk C" using Eq. (2). In Fig. 8 we show how the pk-to-pk C depends on the lateral dimension (a) of the nanopillars for different shapes: Fig. 8(a) for the simulated results and Fig. 8(b) for the experimental results, respectively. We observe that for $a \leq 200$ nm, pk-to-pk $C \to 0$, i.e., we cannot distinguish between the different shapes of the nanopillars. This can also be observed in Figs. 7(b) and 7(c), where for the triangular and square nanopillars with $a \leq 200$ nm, we do not observe any periodicity, and the variation in correlation metric is similar to that of cylindrical nanopillars. This indicates that after $a \leq 200$ nm, we approach the Sommerfeld-Rayleigh system ($a \ll \lambda$), where the nanopillar acts as an oscillating dipole with a defined orientation positioned near the substrate [52]. However for rectangular nanopillars even for $a \leq 200$ nm we always have $b = 1000$ nm, which still influences the far-field signatures, preventing such a regime. Further, we observe that the trends for both the simulated and experimental results demonstrate reasonable agreement, where the metric pk-to-pk C is largest when $a \approx 500$ nm as here we have similar lateral dimensions of the nanopillars and the illuminating focused beam. The results demonstrate that the shape of the nanopillars can be determined for $a \geq 300$ nm.

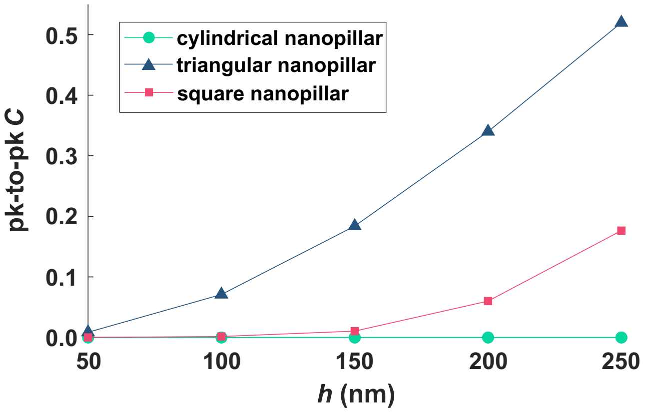

FIG. 9. Limitation analysis of the height (h) of the nanopillars simulated using 3D-FDTD. Indicating that the shape of the square nanopillars can be determined for $h \geq 150$ nm and the shape of the triangular nanopillars can be determined for $h \geq 50$ nm.

Now, we analyze the limitation of the proposed CFS method for the determination of the shape of the nanopillars against the height of the nanopillars. Accordingly, we systematically vary the height of the nanopillars h (=50 nm to 250 nm), for the different shapes of nanopillars (cylindrical, triangular, and square) with $a = 500$ nm. We numerically measure the correlation "C_θ" and calculate the metric "pk-to-pk C" using Eq. (2). In Fig. 9 we show how the pk-to-pk C depends on the height (h) of the nanopillars for different shapes. We observe that pk-to-pk C increases nonlinearly with h, for triangular and square nanopillars. With the triangular nanopillars exhibiting a significantly stronger growth than square nanopillars. Further, we observe that pk-to-pk C is constant (=0) for cylindrical nanopillars, as there is no variation in the correlation metric C_θ. We observe that the shape of the square nanopillars can be determined for $h \geq 150$ nm and the shape of the triangular nanopillars can be determined for $h \geq 50$ nm.

Now, we analyze the limitation of the proposed CFS method for the determination of the shape of the nanopillars against the distortion in the shape of the nanopillars, namely the edge roundness. Accordingly, we introduce

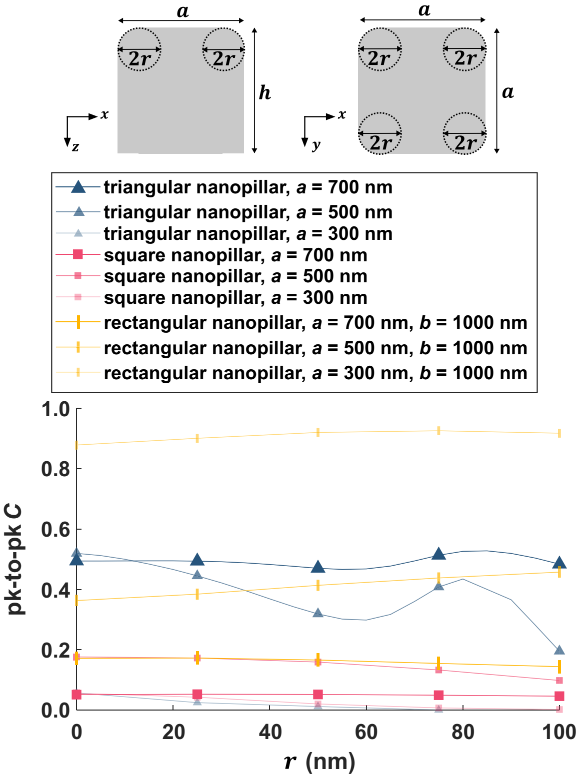

FIG. 10. Limitation analysis of distortion of the shape of the nanopillars simulated using 3D-FDTD. Indicating the robustness of the methodology with the edge roundness (r) of the nanopillars.

edge roundness r (=0 nm to 100) nm (shown schematically in Fig. 10 for a square nanopillar) to the different shapes of the nanopillars (triangular, square, and rectangular) with $a = 300$ nm, 500 nm, and 700 nm, and $h = 250$ nm. We numerically measure the correlation "C_θ" and calculate the metric "pk-to-pk C" using Eq. (2). In Fig. 10 we show how the pk-to-pk C varies with edge roundness (r) of the nanopillars for different shapes. We observe that for all the nanopillars of different shapes pk-to-pk C remains stable. Although we observe some fluctuation for the triangular nanopillar with $a = 500$ nm, pk-to-pk C remains large. Further, only for the triangular and square nanopillars with $a = 300$ nm pk-to-pk C with large edge roundness goes to 0. This is understandable as at this edge roundness, these nanopillars are equivalent to cylindrical nanopillars. These results demonstrate the robustness of the methodology with the variation of edge roundness of the nanopillars.

IV. CONCLUSIONS

In this work, we employed CFS to determine the shapes of various nanopillars, including cylindrical, triangular, square, and rectangular geometries. Both simulations and experiments were conducted for nanopillars with lateral dimensions (a) ranging from 100 to 1000 nm, and the results from both methods showed excellent agreement. Our proposed methodology utilizes the preferential stimulation of an illuminating focused beam and the inherent symmetry of the nanopillars to determine their shapes. By rotating the nanopillars and capturing their far-field signatures, we observed periodic variations in correlations that directly relate to the shape symmetry of the structures. Among the shapes studied, triangular nanopillars exhibited the highest sensitivity to rotation in the far-field measurements. Our method could reliably determine the shape of nanopillars with lateral dimensions $a \geq 300$ nm, which is beyond the conventional diffraction limit of 351 nm. However, for smaller dimensions ($a \leq 200$ nm) we approach the fundamental limitation of our proposed methodology, which was also corroborated by simulations, wherein the nanopillars approach the single dipole approximation regime. This limitation was not observed for rectangular nanopillars, as they have a constant breadth b (=1000 nm) preventing them from reaching this regime. Additionally, our method proved capable of distinguishing nanopillars as they transition from rectangular shape to square shape. We also analyzed the limitations of our approach concerning the height (h) of the nanopillars, finding that triangular nanopillars can be accurately characterized for $h \geq 50$ nm, and square nanopillars for $h \geq 150$ nm. The method was further tested for robustness against shape distortions such as edge roundness (r), showing that it remains effective despite variations up to $r = 100$ nm. However, it is worthwhile to note that this method is limited to determining the lateral (top-down) shape of the nanopillars and cannot resolve longitudinal shape features. Future work will involve expanding this methodology to characterize longitudinal shape features of nanopillars and more intricate shapes. The findings from this study extend the capabilities of CFS to shape determination, potentially leading to advancements in nanofabrication and nanodevice design.

ACKNOWLEDGMENTS

We acknowledge the Nederlandse Organisatie voor Wetenschappelijk Onderzoek (Project 17-24 Synoptics No. 2), and Project 20IND09 "PowerElec" within the program EMPIR; European Commission and the participating countries within the EURAMET for funding this research.

---

[1] W.-Y. Chiu, T.-W. Huang, Y.-H. Wu, Y.-J. Chan, C.-H. Hou, H.-T. Chien, and C.-C. Chen, A photonic crystal ring resonator formed by SOI nano-rods, Opt. Express **15**, 15500 (2007).

[2] H. Butt, Q. Dai, T. D. Wilkinson, and G. A. Amaratunga, Photonic crystals & metamaterial filters based on 2D arrays of silicon nanopillars, Prog. Electromagn. Res. **113**, 179 (2011).

[3] H. Park and K. B. Crozier, Multispectral imaging with vertical silicon nanowires, Sci. Rep. **3**, 2460 (2013).

[4] C. M. Lieber and Z. L. Wang, Functional nanowires, MRS Bull. **32**, 99 (2007).

[5] C. M. Cobley, S. E. Skrabalak, D. J. Campbell, and Y. Xia, Shape-controlled synthesis of silver nanoparticles for plasmonic and sensing applications, Plasmonics **4**, 171 (2009).

[6] M. Khorasaninejad, N. Abedzadeh, J. Walia, S. Patchett, and S. Saini, Color matrix refractive index sensors using coupled vertical silicon nanowire arrays, Nano Lett. **12**, 4228 (2012).

[7] C. Lee, J. Thillaigovindan, C.-C. Chen, X. T. Chen, Y.-T. Chao, S. Tao, W. Xiang, A. Yu, H. Feng, and G. Lo, Si nanophotonics based cantilever sensor, Appl. Phys. Lett. **93**, 113113 (2008).

[8] P. Yang, R. Yan, and M. Fardy, Semiconductor nanowire: What's next? Nano Lett. **10**, 1529 (2010).

[9] R. Kapadia, Z. Fan, K. Takei, and A. Javey, Nanopillar photovoltaics: Materials, processes, and devices, Nano Energy **1**, 132 (2012).

[10] M. Kandziolka, J. J. Charlton, I. I. Kravchenko, J. A. Bradshaw, I. A. Merkulov, M. J. Sepaniak, and N. V. Lavrik, Silicon nanopillars as a platform for enhanced fluorescence analysis, Anal. Chem. **85**, 9031 (2013).

[11] B. R. Murthy, J. Ng, E. Selamat, N. Balasubramanian, and W. Liu, Silicon nanopillar substrates for enhancing signal intensity in DNA microarrays, Biosens. Bioelectron. **24**, 723 (2008).

[12] A. C. Ford, J. C. Ho, Y.-L. Chueh, Y.-C. Tseng, Z. Fan, J. Guo, J. Bokor, and A. Javey, Diameter-dependent electron mobility of InAs nanowires, Nano Lett. **9**, 360 (2009).

[13] D. Ma, C. Lee, F. Au, S. Tong, and S. Lee, Small-diameter silicon nanowire surfaces, Science **299**, 1874 (2003).

[14] B. Tian, P. Xie, T. J. Kempa, D. C. Bell, and C. M. Lieber, Single-crystalline kinked semiconductor nanowire superstructures, Nat. Nanotechnol. **4**, 824 (2009).

[15] S. M. Wells, I. A. Merkulov, I. I. Kravchenko, N. V. Lavrik, and M. J. Sepaniak, Silicon nanopillars for field-enhanced surface spectroscopy, ACS Nano **6**, 2948 (2012).

[16] M. Rippa, R. Castagna, S. Brandi, G. Fusco, M. Monini, D. Chen, J. Zhou, J. Zyss, and L. Petti, Octupolar plasmonic nanosensor based on ordered arrays of triangular Au nanopillars for selective rotavirus detection, ACS Appl. Nano Mater. **3**, 4837 (2020).

[17] V. Fuertes, N. Grégoire, P. Labranche, S. Gagnon, N. Hamada, B. Bellanger, Y. Ledemi, S. LaRochelle, and Y. Messaddeq, Cubic-shaped and rod-shaped YPO4 nanocrystal-doped optical fibers: Implications for next generation of fiber lasers, ACS Appl. Nano Mater. **6**, 4337 (2023).

[18] O. Ergen, D. J. Ruebusch, H. Fang, A. A. Rathore, R. Kapadia, Z. Fan, K. Takei, A. Jamshidi, M. Wu, and A. Javey, Shape-controlled synthesis of single-crystalline nanopillar arrays by template-assisted vapor-liquid-solid process, J. Am. Chem. Soc. **132**, 13972 (2010).

[19] R. Elbersen, W. Vijselaar, R. M. Tiggelaar, H. Gardeniers, and J. Huskens, Fabrication and doping methods for silicon nano-and micropillar arrays for solar-cell applications: A review, Adv. Mater. **27**, 6781 (2015).

[20] L. Golobokova, Y. V. Nastaushev, F. Dultsev, D. Gulyaev, A. Talochkin, and A. Latyshev, Fabrication and optical properties of silicon nanopillars, J. Phys.: Conf. Ser. **541**, 012074 (2014).

[21] S. Kodambaka, J. Tersoff, M. Reuter, and F. Ross, Germanium nanowire growth below the eutectic temperature, Science **316**, 729 (2007).

[22] N. G. Orji, M. Badaroglu, B. M. Barnes, C. Beitia, B. D. Bunday, U. Celano, R. J. Kline, M. Neisser, Y. Obeng, and A. Vladar, Metrology for the next generation of semiconductor devices, Nat. Electron. **1**, 532 (2018).

[23] V. Rodríguez-Fajardo and A. Forbes, Measurement of nanometric heights by modal decomposition, Phys. Rev. Appl. **18**, 064068 (2022).

[24] A. Paul, J. Rafighdoost, X. Dou, and S. F. Pereira, Investigation of coherent Fourier scatterometry as a calibration tool for determination of steep side wall angle and height of a nanostructure, Meas. Sci. Technol. **35**, 075202 (2024).

[25] A. Villegas, M. H. Passos, S. F. Pereira, and J. P. Torres, Optimal parameter estimation of shaped phase objects, Phys. Rev. A **109**, 032617 (2024).

[26] G. Freychet, D. Kumar, R. J. Pandolfi, P. Naulleau, I. Cordova, P. Ercius, C. Song, J. Strzalka, and A. Hexemer, Estimation of line cross sections using critical-dimension grazing-incidence small-angle x-ray scattering, Phys. Rev. Appl. **12**, 044026 (2019).

[27] A. Vella, S. T. Head, T. G. Brown, and M. A. Alonso, Simultaneous measurement of multiple parameters of a subwavelength structure based on the weak value formalism, Phys. Rev. Lett. **122**, 123603 (2019).

[28] N. Kumar, P. Petrik, G. K. Ramanandan, O. El Gawhary, S. Roy, S. F. Pereira, W. M. Coene, and H. P. Urbach, Reconstruction of sub-wavelength features and nano-positioning of gratings using coherent Fourier scatterometry, Opt. Express **22**, 24678 (2014).

[29] P. Van Der Walle, E. Kramer, R. Ebeling, H. Spruit, P. Alkemade, S. Pereira, J. Van Der Donck, and D. Maas, in *Metrology, Inspection, and Process Control for Microlithography XXXII* (SPIE, San Jose, California, United States, 2018), Vol. 10585, p. 570.

[30] S. Krämer, K. Kroth, T. Sure, and P. J. Klar, in *Optical Measurement Systems for Industrial Inspection XIII* (SPIE, Munich, Germany, 2023), Vol. 12618, p. 583.

[31] T. Käseberg, J. Grundmann, T. Siefke, P. Klapetek, M. Valtr, S. Kroker, and B. Bodermann, Mueller matrix ellipsometric approach on the imaging of sub-wavelength nanostructures, Front. Phys. **9**, 814559 (2022).

[32] C. G. Frase, E. Buhr, and K. Dirscherl, CD characterization of nanostructures in SEM metrology, Meas. Sci. Technol. **18**, 510 (2007).

[33] D. Hussain, K. Ahmad, J. Song, and H. Xie, Advances in the atomic force microscopy for critical dimension metrology, Meas. Sci. Technol. **28**, 012001 (2016).

[34] P. Bazylewski, S. Ezugwu, and G. Fanchini, A review of three-dimensional scanning near-field optical microscopy (3D-SNOM) and its applications in nanoscale light management, Appl. Sci. **7**, 973 (2017).

[35] M. H. Madsen and P.-E. Hansen, Scatterometry–fast and robust measurements of nano-textured surfaces, Surf. Topogr.: Metrol. Prop.. **4**, 023003 (2016).

[36] R. J. Kline, D. F. Sunday, D. Windover, and B. D. Bunday, X-ray scattering critical dimensional metrology using a compact x-ray source for next generation semiconductor devices, J. Micro Nanolithogr. MEMS MOEMS **16**, 014001 (2017).

[37] S. Liu, W. Du, X. Chen, H. Jiang, and C. Zhang, Mueller matrix imaging ellipsometry for nanostructure metrology, Opt. Express **23**, 17316 (2015).

[38] C. Wang, X. Chen, C. Chen, S. Sheng, L. Song, H. Gu, H. Jiang, C. Zhang, and S. Liu, Reconstruction of finite deep sub-wavelength nanostructures by Mueller-matrix scattered-field microscopy, Opt. Express **29**, 32158 (2021).

[39] S. Roy, A. C. Assafrao, S. F. Pereira, and H. P. Urbach, Coherent Fourier scatterometry for detection of nanometer-sized particles on a planar substrate surface, Opt. Express **22**, 13250 (2014).

[40] A. Paul, D. Kolenov, T. Scholte, and S. F. Pereira, Coherent Fourier scatterometry: A holistic tool for inspection of isolated particles or defects on gratings, Appl. Opt. **62**, 7589 (2023).

[41] J. J. Stamnes, *Waves in Focal Regions: Propagation, Diffraction and Focusing of Light, Sound and Water Waves* (Routledge, New York, USA, 2017).

[42] J. A. Stratton, *Electromagnetic Theory* (John Wiley & Sons, Hoboken, New Jersey, USA, 2007), Vol. 33.

[43] B. Richards and E. Wolf, Electromagnetic diffraction in optical systems, II. Structure of the image field in an aplanatic system, Proc. R. Soc. London, A **253**, 358 (1959).

[44] R. Dorn, S. Quabis, and G. Leuchs, The focus of light–linear polarization breaks the rotational symmetry of the focal spot, J. Mod. Opt. **50**, 1917 (2003).

[45] A. A. Maradudin, *Light Scattering and Nanoscale Surface Roughness* (Springer Science & Business Media, New York, USA, 2007).

[46] P. Bobbert and J. Vlieger, Light scattering by a sphere on a substrate, Physica A **137**, 209 (1986).

[47] G. W. Videen, W. L. Wolfe, and W. S. Bickel, Light scattering Mueller matrix for a surface contaminated by a single particle in the Rayleigh limit, Opt. Eng. **31**, 341 (1992).

[48] R. Schmehl, B. M. Nebeker, and E. D. Hirleman, Discrete-dipole approximation for scattering by features on surfaces by means of a two-dimensional fast Fourier transform technique, J. Opt. Soc. Am. A **14**, 3026 (1997).

[49] Ansys *Lumerical FDTD solutions*. Available from https://www.lumerical.com/.

[50] L. Novotny and B. Hecht, *Principles of Nano-Optics* (Cambridge University Press, New York, USA, 2012).

[51] İ. R. Çapoğlu, J. D. Rogers, A. Taflove, and V. Backman, The microscope in a computer: Image synthesis from three-dimensional full-vector solutions of Maxwell's equations at the nanometer scale, Prog. Opt. **57**, 1 (2012).

[52] G. Videen, M. G. Turner, V. J. Iafelice, W. S. Bickel, and W. L. Wolfe, Scattering from a small sphere near a surface, JOSA A **10**, 118 (1993).